

Multigrid Predictive Filter Flow for Unsupervised Learning on Videos

Shu Kong, Charless Fowlkes

Dept. of Computer Science, University of California, Irvine

{skong2, fowlkes}@ics.uci.edu

[\[Project Page\]](#), [\[Github\]](#), [\[Demo\]](#), [\[Slides\]](#), [\[Poster\]](#)

Abstract

We introduce multigrid Predictive Filter Flow (mgPFF), a framework for unsupervised learning on videos. The mgPFF takes as input a pair of frames and outputs per-pixel filters to warp one frame to the other. Compared to optical flow used for warping frames, mgPFF is more powerful in modeling sub-pixel movement and dealing with corruption (e.g., motion blur). We develop a multigrid coarse-to-fine modeling strategy that avoids the requirement of learning large filters to capture large displacement. This allows us to train an extremely compact model (**4.6MB**) which operates in a progressive way over multiple resolutions with shared weights. We train mgPFF on unsupervised, free-form videos and show that mgPFF is able to not only estimate long-range flow for frame reconstruction and detect video shot transitions, but also readily amendable for video object segmentation and pose tracking, where it outperforms the state-of-the-art by a notable margin without bells and whistles. Moreover, owing to mgPFF’s nature of per-pixel filter prediction, we have the unique opportunity to visualize how each pixel is evolving during solving these tasks, thus gaining better interpretability¹.

1. Introduction

Videos contain rich information for humans to understand the scene and interpret the world. However, providing detailed per-frame ground-truth labels is challenging for large-scale video datasets, prompting work on leveraging weak supervision such as video-level labels to learn visual features for various tasks [2, 36, 7, 18]. Video constrained to contain primarily ego-motion has also been leveraged for unsupervised learning of stereo, depth, odometry, and optical flow [88, 21, 80, 105, 103].

Cognitively, a newborn baby can easily track an ob-

ject without understanding any high-level semantics by watching the ambient environment for only one month [23, 55, 54, 89]. However, until recently very few work has demonstrated effective unsupervised learning on free-form videos². For example, Wei *et al.* exploit the physics-inspired observation called arrow of time [70, 22] to learn features by predicting whether frames come with the correct temporal order [96], and show the features are useful in action classification and video forensic analysis. Vondrick *et al.* use video colorization as a proxy task and show that the learned features capture objects and parts which are useful for tracking objects [91].

In this paper we explore how to train on unsupervised, free-form videos for video object segmentation and tracking using a new framework we call multigrid Predictive Filter Flow (mgPFF), illustrated by the conceptual flowchart in Fig. 1. mgPFF makes direct, fine-grained predictions of how to reconstruct a video frame from pixels in the previous frame and is trained using simple photometric reconstruction error. We find these pixel-level flows are accurate enough to carry out high-level tasks such as video object segmentation and human pose.

A straightforward approach to learning a flow between frames is to employ a differentiable spatial transform (ST) layer (a.k.a grid sampling) [31], to output per-pixel coordinate offset for sampling pixels with bilinear interpolation and apply the transform to the frame to estimate photometric reconstruction error. This has been widely used in unsupervised optical flow learning [73, 32, 50, 33, 95]. However, we and others observe that unsupervised learning on free-form videos with a simple ST-layer is challenging. Detlefsen *et al.* give an excellent explanation on why it is hard to train with ST-layer in the supervised learning setup [83]. Briefly, training with ST-layer requires the invertibility of the spatial transform which is not guaranteed during train-

¹Due to that arxiv limits the size of files, we put high-resolution figures in the project page.

²By “free-form”, we emphasize the videos are long (versus short synthetic ones [14, 32]), raw and unlabeled, and do not contain either structural pattern (e.g., ego-motion videos [20, 10, 101]) or those with restricted background [87, 75].

ing. Additionally, we note that fixed grids for sampling (usually 2×2 for bilinear interpolation) typically only provide meaningful gradients once the predicted flow is nearly correct (i.e., within 1 pixel of the correct flow). This necessitates training at a coarse scale first to provide a good initialization and avoid getting caught in bad local-minima.

Inspired by the conceptual framework Filter Flow [79], we propose to learn in the mgPFF framework per-pixel filters instead of the per-pixel offset as in the ST-layer. For each output pixel, we predict the weights of a filter kernel that when applied to the input frame reconstruct the output. Conceptually, we reverse the order of operations from the ST-layer. Rather than predicting an offset and then constructing filter weights (via bilinear interpolation), we directly predict filter weights which can vote for the offset vector. We observe that training this model is substantially easier since we get useful gradient information for all possible flow vectors rather than just those near the current prediction.

Since the filter-flow approach outputs per-pixel kernels during training, capturing large displacements is computationally expensive. We address this using a multigrid strategy [86, 24] to approximate the kernel. Concretely, we run the model over multi-resolution inputs with a fixed filter size (11×11 used in this paper) and compose the filters generated at multiple scales to produce the final flow fields (detailed in Section 3.2 and illustrated by Fig. 2). The model thus only outputs $11 \times 11 = 121$ per-pixel filter weights at each resolution scale (smaller than the channel dimension in modern CNN architectures). We further assume self-similarity across scales and learn only a single set of shared learned model weights. This makes our model quite efficient w.r.t running time and model size. As a result, our final (un-optimized) model is only **4.6MB** in size and takes 0.1 seconds to process a pair of 256×256 -pixel resolution images.

To summarize our contributions: (1) conceptually, we introduce a simple multigrid Predictive Filter Flow (mgPFF) framework allowing for unsupervised learning on free-form videos; (2) technically, we show the filter flow overcomes the limitation of spatial-transform layer and the multigrid strategy significantly reduces model size; (3) practically, we show through experiments that mgPFF substantially outperforms other state-of-the-art applications of unsupervised flow learning on challenging tasks including video object segmentation, human pose tracking and long-range flow prediction.

2. Related Work

Unsupervised Learning for Vision: Our work builds upon a flurry of recent work that trains visual models without human supervision. A common approach is to leverage the natural context in images and video for learning the visual

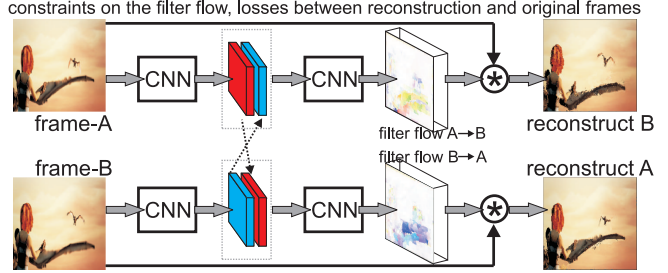


Figure 1: The flowchart of multigrid Predictive Filter Flow framework (mgPFF). Conceptually we draw a single scale for demonstrating how we train our model in an unsupervised way with the photometric reconstruction loss along with constraints imposed on the filter flow maps. The multigrid strategy is illustrated in Fig. 2.

features [12, 62, 34, 13, 93, 104, 41, 65, 92, 90, 61, 64], which can be transferred to down-stream tasks, such as object detection. Other approaches include interaction with an environment to learn visual features [67, 3, 97], which is useful for applications in robotics. A related but different line of work explores how to learn geometric properties or cycle consistencies with self-supervision, for example for motion capture or correspondence [87, 105, 106, 29, 107, 94]. Ours also develop an unsupervised model, but with the signal from temporal consistency between consecutive frames in free-form videos, without the requirement of synthetic data [106, 29].

Unsupervised Learning on Free-Form Videos: Though there are a lot methods for unsupervised optical flow learning [50, 95] on videos (either synthetic [14, 32] or structured [10, 20]), there is very few work about unsupervised learning on free-form videos: [92] uses an offline tracker to provide signal to guide feature learning; [96, 53, 16] learn to verify whether frames come with the correct order, and transfer the feature to action classification; [64] learns for region segmentation on image by considering the moving pattern of rigid objects; [91] learns for video colorization and shows that the learned features capture object or parts which are useful for object tracking; [94] learns correspondence at patch level on videos with reconstruction between frames.

Filter Flow [79] is a powerful framework which models a wide range of low-level vision problems as estimating a spatially varying linear filter. This includes tasks such as optical flow [74, 51, 102], deconvolution [43, 66, 27], non-rigid morphing [57], stereo [78, 49] defocus [45], affine alignment [42], blur removal [26], etc. However, as it requires an optimization-based solver, it is very computationally expensive, requiring several hours to compute filters for a pair of medium-size images [79, 72]. Kong and Fowlkes propose Predictive Filter Flow, which learns to predict per-pixel filters with a CNN conditioned on a single input image

to solve various low-level image reconstruction tasks [39]. There are other methods embracing the idea of predicting per-pixel filters, e.g., [52] and [59] do so for solving burst denoising and video frame interpolation, respectively.

3. Multigrid Predictive Filter Flow

Our multigrid Predictive Filter Flow (mgPFF) is rooted in the Filter Flow framework [79], which models the image transformations $\mathbf{I}_B \rightarrow \mathbf{I}_A$ as a linear mapping where each pixel in \mathbf{I}_A only depends on the local neighborhood centered at same place in \mathbf{I}_B . Finding such a flow of per-pixel filter can be framed as solving a constrained linear system

$$\mathbf{I}_A = \mathbf{T}_{B \rightarrow A} \cdot \mathbf{I}_B, \quad \mathbf{T}_{B \rightarrow A} \in \Gamma. \quad (1)$$

where $\mathbf{T}_{B \rightarrow A}$ is a matrix whose rows act separately on a vectorized version of the source image \mathbf{I}_B . $\mathbf{T}_{B \rightarrow A} \in \Gamma$ serves as a placeholder for the entire set of additional constraints on the operator which enables a unique solution that satisfies our expectations for particular problems of interest. For example, standard convolution corresponds to $\mathbf{T}_{B \rightarrow A}$ being a circulant matrix whose rows are cyclic permutations of a single set of filter weights which are typically constrained to have compact localized non-zero support. For a theoretical perspective, Filter Flow model 1 is simple and elegant, but directly solving Eq. 1 is intractable for image sizes we typically encounter in practice, particularly when the filters are allowed to vary spatially.

3.1. Predictive Filter Flow (PFF) on Video

Instead of optimizing over \mathbf{T} , Kong and Fowlkes propose the Predictive Filter Flow (PFF) framework that learns function $f_{\mathbf{w}}(\cdot)$ parameterized by \mathbf{w} that predicts the transformation \mathbf{T} specific to image \mathbf{I}_B taken as input [39]:

$$\mathbf{I}_A \approx \mathbf{T}_{B \rightarrow A} \cdot \mathbf{I}_B, \quad \mathbf{T}_{B \rightarrow A} \equiv f_{\mathbf{w}}(\mathbf{I}_B), \quad (2)$$

The function $f_{\mathbf{w}}(\cdot)$ is learned with a CNN model under the assumption that $(\mathbf{I}_A, \mathbf{I}_B)$ are drawn from some fixed joint distribution. Therefore, given sampled image pairs, $\{(\mathbf{I}_A^i, \mathbf{I}_B^i)\}$, where $i = 1, \dots, N$, we can learn parameters \mathbf{w} that minimize the difference between a recovered image $\hat{\mathbf{I}}_A$ and the real one \mathbf{I}_A measured by some loss ℓ .

In this work, to tailor the PFF idea to unsupervised learning on videos, under the same assumption that $(\mathbf{I}_A, \mathbf{I}_B)$ are drawn from some fixed joint distribution, we can have the predictable transform $\mathbf{T}_{B \rightarrow A} \equiv f_{\mathbf{w}}(\mathbf{I}_B, \mathbf{I}_A)$, parametrized by \mathbf{w} . To learn the function $f_{\mathbf{w}}(\cdot)$, we use the Charbonnier function [6] to measure the pixel-level reconstruction error, defined as $\phi(s) = \sqrt{s^2 + 0.001^2}$, and learn parameters \mathbf{w} by minimizing the following objective function:

$$\ell_{rec}(\mathbf{I}_B, \mathbf{I}_A) = \phi(\mathbf{I}_A - \mathbf{T}_{B \rightarrow A} \cdot \mathbf{I}_B), \quad (3)$$

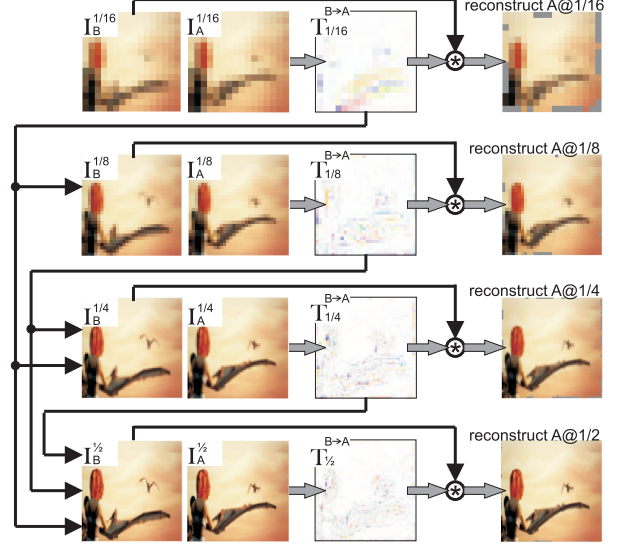


Figure 2: Illustration of how multigrid Predictive Filter Flow (mgPFF) performs progressively by warping images from one to the other at multiple resolution scales from coarse to fine. After the finest scale, one can accumulate all the intermediate filter flow maps for the final one, which can be either transformed into optical flow or used for video segmentation and tracking.

Note that the above loss can take image pairs in different order simply by concatenating the pixel embedding features from the two frames one over another, as demonstrated in Fig. 1. After concatenation, we train a few more layers to produce the per-pixel filters.

Also note that, when exploiting the locality constraints (similar to convolution), we implement the operation $\mathbf{T}_{B \rightarrow A} \cdot \mathbf{I}_B$ with the “im2col” function which vectorizes the local neighborhood patch centered at each pixel and computes the inner product of this vector with the corresponding predicted filter. Note that “im2col” and the follow-up inner product are highly optimized for available hardware architectures in most deep learning libraries, *exactly the same* used in modern convolution operation; thus our model is quite efficient in computation.

3.2. Multigrid PFF

While the PFF described above is elegant and simple for unsupervised learning over videos, it faces the substantial challenge that, to capture large displacement, one must predict per-pixel filters with very large spatial support. To address this problem, we are inspired by the multigrid strategy which seeks to solve high-dimensional systems of equations using hierarchical, multiscale discretizations of linear operators [86, 24], to produce a coarse-to-fine series of smaller, more easily solved problems.

To explain this, mathematically, suppose we have filter flow \mathbf{T} in original resolution that maps from \mathbf{X} to \mathbf{Y} , *i.e.* $\mathbf{Y} = \mathbf{T} \cdot \mathbf{X}$. Then if we downsample \mathbf{X} and \mathbf{Y} by half, we

have

$$\mathbf{D}_{\frac{1}{2}} \mathbf{Y} = \mathbf{D}_{\frac{1}{2}} \mathbf{T} \cdot \mathbf{X} \approx (\mathbf{D}_{\frac{1}{2}} \mathbf{T}) \cdot (\mathbf{U}_{2\times} \mathbf{D}_{\frac{1}{2}} \mathbf{X}), \quad (4)$$

where the upsampling $\mathbf{U}_{2\times}$ and downsampling $\mathbf{D}_{\frac{1}{2}}$ operators are approximately inverse to each other. Then we write a reduced system:

$$\mathbf{Y}_{\frac{1}{2}} \approx (\mathbf{D}_{\frac{1}{2}} \mathbf{T} \mathbf{U}_{2\times}) \cdot (\mathbf{D}_{\frac{1}{2}} \mathbf{X}) = \mathbf{T}_{\frac{1}{2}} \mathbf{X}_{\frac{1}{2}} \quad (5)$$

The above derivation implies we can solve a smaller system for $\mathbf{T}_{\frac{1}{2}}$ on the input $\mathbf{X}_{\frac{1}{2}}$, e.g., an image with half the resolution and then upsample $\mathbf{T}_{\frac{1}{2}}$ to get an approximate solution to the original problem.

In practice, to avoid assembling the full resolution \mathbf{T} , we always represent it as a composition of residual transformations at each scale. $\mathbf{T} = \mathbf{T}_1 \cdot \mathbf{U}_{2\times} \cdot \mathbf{T}_{\frac{1}{2}} \dots \mathbf{U}_{2\times} \cdot \mathbf{T}_{\frac{1}{2^L}}$, where $\mathbf{T}_{\frac{1}{2^L}}$ is estimated filter flow over frames at resolution scale $1/2^{L-1}$. In our work, we set $L=5$. Each individual transformation has a fixed filter support (sparse). By construction, the effective filter “sizes” grow spatially larger as it goes up in the pyramid but the same filter weight is simply applied to larger area (we use nearest-neighbor upsampling). Then the total number of filter coefficients to be predicted for the pyramid would be just 4/3 more than just the finest level (ref. geometric series $4/3 = 1 + \frac{1}{2^2} + \frac{1}{4^2} + \frac{1}{8^2} + \dots$).

Concretely, suppose we need the kernel size as 80×80 to capture large displacement, we can work on coarse scale of $8 \times$ smaller input region with kernel size 11×11 , this will reflect on the original image of receptive field as large as 88×88 . But merely working on such coarse scale introduces checkerboard effect if we resize the filters $8 \times$ larger. Therefore, we let the model progressively generate a series of 11×11 filters at smaller scales of $[8 \times, 4 \times, 2 \times, 1 \times]$, as demonstrated by Fig. 2. Finally, we can accumulate all the generated filter flows towards the single map, which can be a long-range flow (studied in Section 4.4). We train our system with the same model at all these scales. We have also trained scale-specific models, but we do not observe any obvious improvements in our experiments. We conjecture that in diverse, free-form videos there is substantial self-similarity in the (residual) flow across scales.

We note that coarse-to-fine estimation of residual motion is a classic approach to estimating optical flow (see, e.g. [17]). It has also been used to handle problems of temporal aliasing [81] and as a technique for imposing a prior smoothness constraint [85]. Framing flow as a linear operator draws a close connection to multigrid methods in numerical analysis [86, 24]. However, in literature there is primarily focused on solving for \mathbf{X} where the residuals are additive, rather than \mathbf{T} where the residuals are naturally multiplicative.

3.3. Imposing Constraints and Training Loss

We note that training with above reconstruction loss alone gives very good reconstruction performance, but we need other constraints to regularize training to make it work on video segmentation and tracking. Now we describe useful constraints used in this work.

Non-negativity and Sum-to-One With the PFF framework, it is straightforward to impose the non-negativity and sum-to-one constraints by using the softmax layer to output the per-pixel filters, as softmax operation on the kernels naturally provides a transformation on the weights into the range of $[0, 1]$, and sum-to-one constraint mimics the brightness constancy assumption of optical flow.

Warping with Flow Vector In order to encourage the estimated filter kernels to behave like optical flow (i.e., a translated delta function) we define a projection of the filter weights on to the best approximate flow vector by treating the (positive) weights as a distribution and computing an expectation. Given a filter flow \mathbf{T} we define the nearest optical flow as

$$\mathbf{F}(\mathbf{T}) \equiv \begin{bmatrix} v_x(i, j) \\ v_y(i, j) \end{bmatrix} = \sum_{x, y} T_{ij, xy} \begin{bmatrix} x - i \\ y - j \end{bmatrix} \quad (6)$$

As discussed in Section 1, directly learning to predict \mathbf{F} is difficult but when keep \mathbf{T} as an intermediate representation, learning becomes much easier. To encourage predicted \mathbf{T} towards a unimodal offset, we add a loss term based on the optical flow \mathbf{F} with grid sampling layer just as done in literature of unsupervised optical flow learning [73, 95, 32]. We denote the loss terms as $\ell_{flow}(\mathbf{I}_B, \mathbf{I}_A)$ meaning the reconstruction loss computed by warping with optical flow $\mathbf{F}(\mathbf{T}_{B \rightarrow A})$ from \mathbf{I}_B to \mathbf{I}_A .

Forward-Backward Flow Consistency As we know, there are many solutions to the reconstruction problem. To constrain this for more robust learning, we adopt a forward-backward consistency constraint as below:

$$\ell_{fb}(\mathbf{f}, \mathbf{b}) \equiv \frac{1}{|\mathcal{I}|} \sum_{i \in \mathcal{I}} \phi(\mathbf{p}_i - \mathbf{b}(\mathbf{f}(\mathbf{p}_i))) \quad (7)$$

where forward and backward flow are $\mathbf{f} = \mathbf{F}(\mathbf{T}_{B \rightarrow A})$ and $\mathbf{b} = \mathbf{F}(\mathbf{T}_{A \rightarrow B})$, and $\mathbf{p}_i \equiv [x_i, y_i]^T$ is the spatial coordinate. We note that such constraint is useful for addressing the chicken-and-egg problem related to optical flow and occlusion/disocclusion [28, 50]. But here we do not threshold the consistency error to find occlusion regions or ignore the errors in the region. We note that it is crucial to train the mgPFF model with this constraint when applying the model later for video segmentation and tracking; otherwise pixels in the object would diffuse to the background easily.

Smoothness and Sparsity Smoothness constraints can be done easily using traditional penalties on the norm of the flow field gradient, i.e. $\ell_{sm} \equiv \|\nabla \mathbf{F}(\mathbf{T})\|_1$. The smoothness

penalty helps avoid big transitions on flow field, especially at coarse scales where very few big flows are expected. The sparsity constraint is imposed on the flow field as well with L1 norm, *i.e.* $\ell_{sp} \equiv \|\mathbf{F}(\mathbf{T})\|_1$. This forces the model not to output too many abrupt flows especially at finer scales.

Our overall loss for training mgPFF model minimizes the following combination of the terms across multiple scales $l = 1 \dots, L$:

$$\begin{aligned} \min_{\mathbf{w}} \sum_{l=1}^L & \ell_{rec}(\mathbf{I}_B^l, \mathbf{I}_A^l) + \lambda_{fl} \cdot \ell_{fl}(\mathbf{I}_B^l, \mathbf{I}_A^l) \\ & + \lambda_{fb} \cdot \ell_{fb}(\mathbf{f}^l, \mathbf{b}^l) + \lambda_{sm} \cdot \ell_{sm}(\mathbf{f}^l) + \lambda_{sp} \cdot \ell_{sp}(\mathbf{f}^l) \quad (8) \\ \text{s.t.} \quad & \mathbf{T}_{B \rightarrow A}^l = \mathbf{f}_{\mathbf{w}}(\mathbf{I}_B^l, \mathbf{I}_A^l), \mathbf{T}_{A \rightarrow B}^l = \mathbf{f}_{\mathbf{w}}(\mathbf{I}_A^l, \mathbf{I}_B^l), \\ & \mathbf{f}^l = \mathbf{F}(\mathbf{T}_{B \rightarrow A}^l), \mathbf{b}^l = \mathbf{F}(\mathbf{T}_{A \rightarrow B}^l). \end{aligned}$$

For simplicity, we only write the losses involving flow from B to A ; in practice, we also include those A to B .

3.4. Implementation and Training

Our basic framework is largely agnostic to the choice of architectures. In this paper, we modify the ResNet18 [25] by removing res_4 and res_5 (the top 9 residual blocks, see appendix) and reducing the unique channel size from [64, 128, 256, 512] to [32, 64, 128, 196]. We also add in bilateral connection and upsampling layers to make it a U-shape [77], whose output is at the original resolution. Furthermore, we build another shallow stream but in full-resolution manner with batch normalization [30] between a convolution layer and ReLU layer [56] that learns to take care of aliasing effect caused by pooling layers in the first steam. We note that our mgPFF is very compact that the overall model size is only **4.6MB**; it also performs fast that the wall-clock time for processing a pair of 256x256 frames is 0.1 seconds. Two-stream architecture is popular in multiple domain learning [82], but we note that such design on a single domain was first used in [68] which is more computationally expensive that the two streams talk to each other along the whole network flow; whereas ours is cheaper that they only talk at the top layer. We note that our architecture is different from FlowNetS and FlowNetC [14] in that, 1) unlike FlowNetS, ours produces pixel embedding features for each of frame, which can be potentially transferred to other tasks (though we did not explore this under the scope of this paper); 2) unlike FlowNetC, ours does not exploit the computationally expensive correlation layer.

4. Experiments

We conduct experiments to show the mgPFF can be trained in an unsupervised learning fashion on diverse, free-form videos, and applicable to addressing challenging tasks including video object segmentation, pose tracking and long-range flow learning in terms of frame reconstruction.

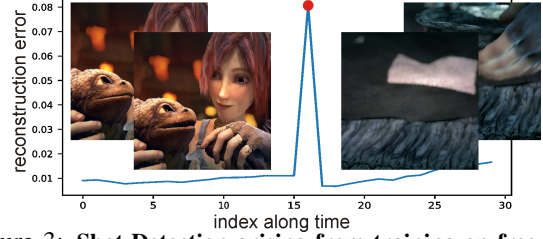


Figure 3: **Shot Detection arising from training on free-form videos:** By training our mgPFF on the Sintel movie, we can detect the transition shot purely based on the reconstruction error. This helps develop a stage-wise training that we train mgPFF first on the whole movie, and then simply threshold the reconstruction errors for shot detection and get discrete groups for finer training.

We also visualize how each pixel evolves during solving these problems to gain better interpretability of the model.

We evaluate our mgPFF model on the challenging video propagation tasks: DAVIS2017 [69] for video object segmentation and long-range flow learning in terms of frame reconstruction, and JHMDB dataset [35] for human pose tracking.

Compared methods include the simplistic identity mapping (always copying the first frame labels), SIFT flow [46] which is an off-the-shelf toolbox for dense correspondence alignment, learning-based optical flow (FlowNet2) [29] which is trained on large-scale synthetic data, DeepCluster [9] which is unsupervised trained for clustering on ImageNet [11], ColorPointer [91] which learns video colorization and shows effective in object tracking, and CycleTime [94] which exploits the cycle consistence along time and is trained for patch reconstruction with mid-level feature activations.

4.1. Experimental Setup

Training. We train our mgPFF model from scratch over a combined datasets consisting of the whole Sintel Movie [44], training set of DAVIS2017 [69], and training set of JHMDB (split1) [35]. It is worth noting that our whole training set contains only $\sim 6 \times 10^4$ frames, whereas our compared methods train over orders magnitude larger dataset. For example, ColorPointer [91] is trained over 300K videos ($\sim 9 \times 10^7$ frames) from Kinetics dataset [36], and CycleTime [94] is trained over 114K videos (344-hour recording, $\sim 3.7 \times 10^7$ frames) from VLOG dataset [18]. Moreover, most interestingly, in training our mgPFF on the Sintel movie, we find mgPFF automatically learns to detect the video shot/transition [5, 19] purely based on the reconstruction errors between input frames (see Fig. 3).

We use ADAM optimization method during training [38], with initial learning 0.0005 and coefficients 0.9 and 0.999 for computing running averages of gradient and its square. We randomly initialize the weights and train from scratch over free form videos. We train our model

Table 1: **Tracking Segmentation** on the DAVIS2017 validation set. Methods marked with ^{1st} additionally use the first frame and its mask (provided) for tracking in the rest of the video. The **number** in bracket is the estimated number of frames used for training the corresponding method.

Method	Supervision	\mathcal{J} (segments)		\mathcal{F} (boundaries)	
		mean \uparrow	recall \uparrow	mean \uparrow	recall \uparrow
OSVOS [8]	ImageNet, DAVIS	55.1	60.2	62.1	71.3
MaskTrack [37]	ImageNet, DAVIS	51.2	59.7	57.3	65.5
OSVOS-B [8]	ImageNet	18.5	15.9	30.0	20.0
MaskTrack-B [37]	ImageNet	35.3	37.8	36.4	36.0
OSVOS-M [99]	ImageNet	36.4	34.8	39.5	35.3
Identity	None	22.1	15.9	23.6	11.7
SIFTflow [46]	None	13.0	7.9	15.1	5.5
SIFTflow ^{1st} [46]	None	33.0	—	35.0	—
FlowNet2 [29]	Synthetic	16.7	9.5	19.7	7.6
FlowNet2 ^{1st} [29]	Synthetic	26.7	—	25.2	—
DeepCluster ^{1st} [9]	Self (1.3×10^6)	37.5	—	33.2	—
ColorPointer [91]	Self (9.0×10^7)	34.6	34.1	32.7	26.8
CycleTime ^{1st} [94]	Self (3.7×10^7)	40.1	—	38.3	—
mgPFF (1st only)	Self (6.0×10^4)	31.6	29.5	36.2	30.8
mgPFF ($K=1$)		38.9	38.5	41.1	38.6
mgPFF ^{1st} ($K=1$)		41.9	41.4	45.2	43.9
mgPFF ^{1st} ($K=3$)		42.2	41.8	46.9	44.4

using PyTorch [63] on a single NVIDIA TITAN X GPU, and terminate after 500K iteration updates.³ During training, we randomly sample frame pairs (resized to 256×256 -pixel resolution) within $N=5$ consecutive frames. We also augment the training set by randomly flipping and rotating the frame pairs. After training the model on the combined dataset, we train specifically over the training set (without annotation) of DAVIS2017 and JHMDB respectively for video object segmentation and human pose tracking.

Inference. We essentially propagate the given mask/pose at the first frame along the time. We also set the temporal window size K , meaning we warp towards the target frame using previous K frames. We test different temporal window size for video segmentation and tracking and find $K=3$ works the best. Specifically, for video object segmentation on DAVIS2017, we threshold with 0.8 the propagated mask at each tracking update, since pixels on the foreground (within the mask) may diffuse to background, and filter flow gives probabilities around the mask boundary. For human pose tracking, we dilate the joints for propagation, and vote for the tracked joint after propagation as the track. This gives stable tracking though sometimes the track may stay at the background especially when the background is similar to the foreground (3rd video in Fig. 5). We note that there are other methods using low-level cues for higher-level tasks, e.g., using boundary for semantic segmentation [4, 47].

4.2. Unsupervised Learning for Video Segmentation

We analyze our model on video segmentation over the DAVIS 2017 validation set [69], where the initial segmentation mask is given and the task is to predict the segmentation in the rest of the video. This is a very challenging task as the videos contain multiple objects that undergo significant occlusion, deformation and scale change with clutter background, as shown in Fig. 4. We use the provided code and report two metrics that score segment overlap and boundary accuracy. The Jaccard index \mathcal{J} is defined as the intersection-over-union of the estimated segmentation and the ground-truth mask, measuring how well the pixels of two masks match [15]. The \mathcal{J} recall measures the fraction of sequences with $\text{IoU} > 0.5$. The F-measure denoted by \mathcal{F} considers both contour-based precision and recall that measure the accuracy of the segment contours [48].

We compare our mgPFF with other unsupervised methods as well as some supervised ones [99, 8] in Table 1. The first two supervised methods are trained explicitly using the annotated masks along with training video frames. As in literature there are methods always using the given mask at the first frame to aid tracking, we also follow this practice with mgPFF to report the performance. But before doing so, we ablate how much gain we can get from using only the given mask for the tracking. To this end, we setup the mgPFF by always propagating the given mask for tracking, as noted by mgPFF (1st only) in Table 1. Surprisingly, this simple setup works very well, even better than flow based methods, such as SIFTflow^{1st} and FlowNet2^{1st}, both of which not only use the first frame but also the previous $N=4$ frames for tracking. This suggests the mgPFF is able to capture long-range flow even though we did not train our model with frames across large intervals. We explicitly study this long-range flow in Section 4.4 quantitatively.

When we perform tracking with the *only one* previous propagated mask ($K=1$), our mgPFF outperforms all the other unsupervised methods, except CycleTime (on \mathcal{J} measure only), which is explicitly trained at patch level thus captures better object segment. When additionally using the mask given at the first frame for tracking in subsequent frames, mgPFF^{1st} ($K=1$) outperforms all other unsupervised methods by a notable margin, and our mgPFF^{1st} ($K=3$) achieves the best performance. In particular, in terms of the boundary measure, we can see mgPFF performs significantly better than the other unsupervised methods. This demonstrates the benefit of propagating masks with fine-grained pixel-level flows instead of flows learned at patch level through mid-level feature activations [91, 94].

Overall, we note that our mgPFF even outperforms sev-

³ The code and models can be found in <https://github.com/aimerykong/predictive-filter-flow>



Figure 4: Visualization of unsupervised learning for video segmentation on video from DAVIS2017: *soccerball*, *dog* and *bear*. We show the tracking results with temporal window size $K=3$ for *soccerball* (otherwise it loses track due to heavy occlusion) and $K=1$ for others. Note that in *soccerball*, there are heavy occlusions but our mgPFF model can still track the ball. In *dog*, we can see how each pixel moves along with the dog: when the dog turns from right side to left side, the colors from the neck are propagated for tracking. This demonstrates how mgPFF tracks each pixel in the physical manifold flavor. In *bear*, the disocclusion shadow arises from the bottom border of the image, connecting with the bear, then mgPFF propagates the bear leg to the shadow.

eral supervised methods, but only worse than the first two supervised models in Table 1 which are explicitly trained with DAVIS pixel-level annotations at all training frames. Moreover, it is worth noting that our mgPFF model is trained over two orders magnitude less data than other unsupervised methods, e.g., DeepCluster, ColorPointer and CycleTime. This demonstrates the benefit brought by the low-vision nature of mgPFF that it does not demand very large-scale training data.

In Fig. 4, we visualize the tracking results ($N=3$) and the predicted filter flow (from previous one frame only). Specifically, we transform the filter flow into the flow vector (Eq. 6) and treat this as optical flow for visualization. As mgPFF performs at pixel level, we are able to visualize the tracking through more fine-grained details. We paint on the mask with the color chart from optical flow, and visualize to see how the pixels evolve over time. Interestingly, from this visualization, we can see how tracking is accomplished in front of heavy occlusion, big deformation and similar background situation (see descriptions under Fig. 4).

4.3. Unsupervised Learning for Pose Tracking

We validate our mgPFF for human pose tracking on the JHMDB dataset [35]. During testing, we are given an initial frame labeled with 15 human joints and the task is to predict the joints in the subsequent frames. To this end, we stack the 15 maps for the 15 joints as a 3D array, and propagate the array using the predicted filter flow. To report performance, we use the Probability of Correct Keypoint (PCK@ τ) from [100], which measures the portion of predicted points that are within a radius to their ground-truth, where the radius is τ times the size of the human pose bounding box.

In Table 2 we list the performance of different unsupervised learning methods, and report two setups of the mgPFF

Table 2: **Human Pose Tracking** on JHMDB dataset. Methods marked with ^{1st} additionally use the first frame with its mask for propagating on the rest frames. “mgPFF+ft” means that we fine-tune mgPFF model particularly on the videos from this dataset in an unsupervised way (no annotations used).

Method / PCK \uparrow	@0.1	@0.2	@0.3	@0.4	@0.5
fully-supervised [84]	68.7	92.1			
Identity	43.1	64.5	76.0	83.5	88.5
SIFTflow ^{1st} [46]	49.0	68.6	—	—	—
FlowNet2 [29]	45.2	62.9	73.5	80.6	85.5
DeepCluster ^{1st} [9]	43.2	66.9			
ColorPointer [91]	45.2	69.6	80.8	87.5	91.4
CycleTime ^{1st} [94]	57.3	78.1	—	—	—
mgPFF	49.3	72.8	82.4	88.6	91.9
mgPFF ^{1st}	55.6	77.1	85.2	89.6	92.1
mgPFF+ft	52.7	75.1	84.0	89.5	92.3
mgPFF+ft ^{1st}	58.4	78.1	85.9	89.8	92.4

on the validation set (split1): 1) with the model trained on the combined dataset, and 2) with the model further fine-tuned on JHMDB in an unsupervised way [71, 95, 27]. Similar to video segmentation, without using the provided joints at the first frame for all subsequent tracking, our mgPFF outperforms all other methods except CycleTime which always uses the first frame (with the provided keypoints) for pose tracking. By fine-tuning our model on the videos of this dataset (without using the joint annotations), we obtain further improvement; but the improvement is less than additionally using the first frame for tracking. We conjecture the reason is that by using the provided mask at the first frame, mgPFF is able to warp all the available joints toward current frame; otherwise it may lose track once the joints move outside the image (see 2nd video in Fig. 5). It is worth noting that mgPFF as well as the learning based optical flow

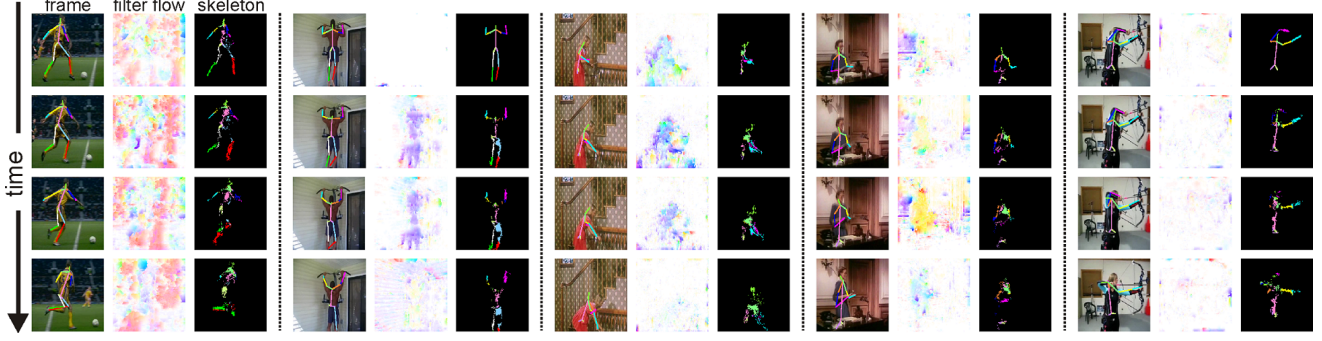


Figure 5: **Human Pose Tracking** on JHMDB dataset. We show results by propagating only the previous mask ($K=1$), and overlay the tracked joints on the RGB frames. Besides, with the predicted filter flow, we also propagate the colorful skeleton to visualize how pixels on the skeleton evolve over time. In last row, we pick the results around the end of each video to show how mgPFF fails in tracking, mainly due to heavy occlusion (knees in the 1st video), joints moving outside the image (ankle in the 2nd video), similar background (hair color in the 3rd video), and motion blur (elbow in the 4th video). (Best viewed in color and zoom-in.)

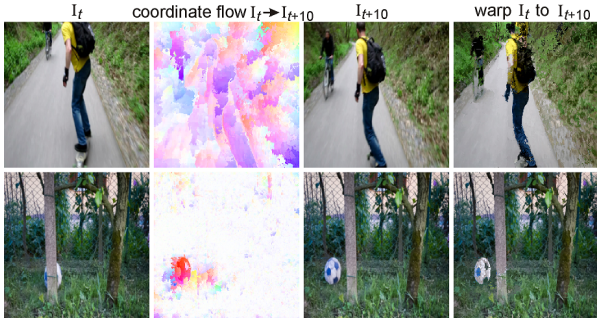


Figure 6: **Long-range flow for frame reconstruction** (rightmost column) by warping I_t (1st column) with the coordinate flow (2nd column) which is transformed from the predicted multigrid filter flow. The target frames I_{t+10} are shown in the 3rd column.

method performs fast in propagating the joints for tracking, whereas DeepCluster, ColorPointer and CycleTime require computing affinity matrix over all pixels from previous K frames [91, 94]. Moreover, although it seems unfair to compare our mgPFF with unsupervised fine-tuning on the same JHMDB dataset, we note that ColorPointer and CycleTime are trained on much larger dataset consisting mainly of human actions/activities.

In Fig. 5, we visualize the pose tracking results as well as the filter flow and how each pixel along the skeleton evolves over time. We plot in last row the frames on which our mgPFF starts to fail in tracking. The failure cases are largely due to challenging situations, like heavy occlusion (1st video), joint moving outside the image, similar background (3rd video) and big motion blur (4th video).

4.4. Long-Range Flow for Frame Reconstruction

We highlight our mgPFF is particularly good at learning long-range flow for reconstructing frames. To validate this, specifically, given two frames I_t and I_{t+m} distant in time in a video, we predict the filter flow between them, and then

Table 3: **Long-range flow for frame Reconstruction**: We compute the long-range flow on two frames and warp the 1st one with the flow. We compare the warped frame with the 2nd frame measured by pixel-level L1 distance. The gaps are 5 and 10, respectively.

method/error↓	5-Frame	10-Frame
Identity	82.0	97.7
Optical Flow (FlowNet2) [29]	62.4	90.3
CycleTime [94]	60.4	76.4
mgPFF	7.32	8.83

transform the filter flow into coordinate flow according to Eq. 6 to indicate where to copy pixels from I_t . With the coordinate flow, we warp frame I_t to generate a new frame \hat{I}_{t+m} . We compare the pixel-level L1 distance between I_t and \hat{I}_{t+m} in original uint8 RGB space ($[0,255]$ scale).

We perform this experiment on DAVIS2017 validation set, and report the performance in Table 3, in which we set the time gap as $m=5$ or $m=10$, meaning the two frames are m frames apart from each other. In both frame gaps, our mgPFF significantly outperforms the compared methods, demonstrating the powerfulness of mgPFF in modeling pixel level movement, even though our model is trained over frame pairs within 5-frame interval without seeing any frames far away from 5 frames. In Fig. 6, we clearly see that mgPFF performs quite well visually on long-range flow learning for frame reconstruction.

5. Conclusion

We propose a simple, compact framework for unsupervised learning on free-form videos, named multigrid Predictive Filter Flow (mgPFF). Through experiments, we show mgPFF outperforms other state-of-the-art methods notably in video object segmentation and human pose tracking with the unsupervised learning setup; it also exhibits great power in long-range flow learning in terms of frame re-

construction. In this sense, it is reminiscent of a variety of other flow-based tasks, such as video compression [76], frame interpolation [60], unsupervised optical flow learning [101, 32], etc., which are all candidates for future extensions. Moreover, based on the filter flow output which is fast in computation, it is also interesting to use it for action classification where the flow stream consistently improves performance [82] but optical flow estimation is slow. Finally the pixel embedding features [40, 96] could also be used as video frame representation for action classification [53, 16]. We expect further improvement on these tasks by taking as mgPFF as initial proposal generation with followup mechanisms for fine video segmentation [98, 91, 94, 64].

Acknowledgement

This project is supported by NSF grants IIS-1813785, IIS-1618806, IIS-1253538 and a hardware donation from NVIDIA. Shu Kong personally thanks Teng Liu and Etthew Kong who initiated this research, and the academic uncle Alexei A. Efros for the encouragement and discussion.

References

- [1] W. Abdulla and P. Ferriere. Neural network graphs and training metrics for pytorch and tensorflow. 2018. [13](#), [15](#)
- [2] S. Abu-El-Haija, N. Kothari, J. Lee, P. Natsev, G. Toderici, B. Varadarajan, and S. Vijayanarasimhan. Youtube-8m: A large-scale video classification benchmark. *arXiv preprint arXiv:1609.08675*, 2016. [1](#)
- [3] P. Agrawal, A. V. Nair, P. Abbeel, J. Malik, and S. Levine. Learning to poke by poking: Experiential learning of intuitive physics. In *Advances in Neural Information Processing Systems*, pages 5074–5082, 2016. [2](#)
- [4] P. Arbelaez, M. Maire, C. Fowlkes, and J. Malik. Contour detection and hierarchical image segmentation. *IEEE transactions on pattern analysis and machine intelligence*, 33(5):898–916, 2011. [6](#)
- [5] J. S. Boreczky and L. A. Rowe. Comparison of video shot boundary detection techniques. *Journal of Electronic Imaging*, 5(2):122–129, 1996. [5](#)
- [6] A. Bruhn and J. Weickert. Towards ultimate motion estimation: Combining highest accuracy with real-time performance. In *10th IEEE International Conference on Computer Vision (ICCV 2005), 17-20 October 2005, Beijing, China*, pages 749–755, 2005. [3](#)
- [7] F. Caba Heilbron, V. Escorcia, B. Ghanem, and J. Carlos Nieves. Activitynet: A large-scale video benchmark for human activity understanding. In *Proceedings of the IEEE Conference on Computer Vision and Pattern Recognition*, pages 961–970, 2015. [1](#)
- [8] S. Caelles, K.-K. Maninis, J. Pont-Tuset, L. Leal-Taixé, D. Cremers, and L. Van Gool. One-shot video object segmentation. In *Proceedings of the IEEE conference on computer vision and pattern recognition*, pages 221–230, 2017. [6](#)
- [9] M. Caron, P. Bojanowski, A. Joulin, and M. Douze. Deep clustering for unsupervised learning of visual features. In *Proceedings of the European Conference on Computer Vision (ECCV)*, pages 132–149, 2018. [5](#), [6](#), [7](#)
- [10] M. Cordts, M. Omran, S. Ramos, T. Rehfeld, M. Enzweiler, R. Benenson, U. Franke, S. Roth, and B. Schiele. The cityscapes dataset for semantic urban scene understanding. In *Proceedings of the IEEE conference on computer vision and pattern recognition*, pages 3213–3223, 2016. [1](#), [2](#)
- [11] J. Deng, W. Dong, R. Socher, L.-J. Li, K. Li, and L. Fei-Fei. ImageNet: A Large-Scale Hierarchical Image Database. In *CVPR09*, 2009. [5](#)
- [12] C. Doersch, A. Gupta, and A. A. Efros. Unsupervised visual representation learning by context prediction. In *Proceedings of the IEEE International Conference on Computer Vision*, pages 1422–1430, 2015. [2](#)
- [13] C. Doersch and A. Zisserman. Multi-task self-supervised visual learning. In *Proceedings of the IEEE International Conference on Computer Vision*, pages 2051–2060, 2017. [2](#)
- [14] A. Dosovitskiy, P. Fischer, E. Ilg, P. Hausser, C. Hazirbas, V. Golkov, P. Van Der Smagt, D. Cremers, and T. Brox. FlowNet: Learning optical flow with convolutional networks. In *Proceedings of the IEEE International Conference on Computer Vision*, pages 2758–2766, 2015. [1](#), [2](#), [5](#)
- [15] M. Everingham, L. Van Gool, C. K. Williams, J. Winn, and A. Zisserman. The pascal visual object classes (voc) challenge. *International journal of computer vision*, 88(2):303–338, 2010. [6](#)
- [16] B. Fernando, H. Bilen, E. Gavves, and S. Gould. Self-supervised video representation learning with odd-one-out networks. In *Proceedings of the IEEE conference on computer vision and pattern recognition*, pages 3636–3645, 2017. [2](#), [8](#)
- [17] D. Fleet and Y. Weiss. Optical flow estimation. In *Handbook of mathematical models in computer vision*, pages 237–257. Springer, 2006. [4](#)
- [18] D. F. Fouhey, W.-c. Kuo, A. A. Efros, and J. Malik. From lifestyle vlogs to everyday interactions. In *Proceedings of the IEEE Conference on Computer Vision and Pattern Recognition*, pages 4991–5000, 2018. [1](#), [5](#)
- [19] U. Gargi, R. Kasturi, and S. H. Strayer. Performance characterization of video-shot-change detection methods. *IEEE transactions on circuits and systems for video technology*, 10(1):1–13, 2000. [5](#)
- [20] A. Geiger, P. Lenz, C. Stiller, and R. Urtasun. Vision meets robotics: The kitti dataset. *The International Journal of Robotics Research*, 32(11):1231–1237, 2013. [1](#), [2](#)
- [21] C. Godard, O. Mac Aodha, and G. J. Brostow. Unsupervised monocular depth estimation with left-right consistency. In *Proceedings of the IEEE Conference on Computer Vision and Pattern Recognition*, pages 270–279, 2017. [1](#)
- [22] T. Gold. The arrow of time. *American Journal of Physics*, 30(6):403–410, 1962. [1](#)
- [23] C. C. Goren, M. Sarty, and P. Y. Wu. Visual following and pattern discrimination of face-like stimuli by newborn infants. *Pediatrics*, 56(4):544–549, 1975. [1](#)

- [24] W. Hackbusch. *Multi-grid methods and applications*, volume 4. Springer Science & Business Media, 2013. 2, 3, 4
- [25] K. He, X. Zhang, S. Ren, and J. Sun. Deep residual learning for image recognition. In *Proceedings of the IEEE conference on computer vision and pattern recognition*, pages 770–778, 2016. 5, 13
- [26] M. Hirsch, C. J. Schuler, S. Harmeling, and B. Schölkopf. Fast removal of non-uniform camera shake. In *2011 International Conference on Computer Vision*, pages 463–470. IEEE, 2011. 2
- [27] M. Hirsch, S. Sra, B. Schölkopf, and S. Harmeling. Efficient filter flow for space-variant multiframe blind deconvolution. In *2010 IEEE Computer Society Conference on Computer Vision and Pattern Recognition*, pages 607–614. IEEE, 2010. 2, 7
- [28] J. Hur and S. Roth. Mirrorflow: Exploiting symmetries in joint optical flow and occlusion estimation. In *Proceedings of the IEEE International Conference on Computer Vision*, pages 312–321, 2017. 4
- [29] E. Ilg, N. Mayer, T. Saikia, M. Keuper, A. Dosovitskiy, and T. Brox. FlowNet 2.0: Evolution of optical flow estimation with deep networks. In *Proceedings of the IEEE Conference on Computer Vision and Pattern Recognition*, pages 2462–2470, 2017. 2, 5, 6, 7, 8
- [30] S. Ioffe and C. Szegedy. Batch normalization: Accelerating deep network training by reducing internal covariate shift. *arXiv preprint arXiv:1502.03167*, 2015. 5
- [31] M. Jaderberg, K. Simonyan, A. Zisserman, et al. Spatial transformer networks. In *Advances in neural information processing systems*, pages 2017–2025, 2015. 1
- [32] J. Janai, F. Guney, A. Ranjan, M. Black, and A. Geiger. Unsupervised learning of multi-frame optical flow with occlusions. In *Proceedings of the European Conference on Computer Vision (ECCV)*, pages 690–706, 2018. 1, 2, 4, 8
- [33] J. Y. Jason, A. W. Harley, and K. G. Derpanis. Back to basics: Unsupervised learning of optical flow via brightness constancy and motion smoothness. In *European Conference on Computer Vision*, pages 3–10. Springer, 2016. 1
- [34] D. Jayaraman and K. Grauman. Learning image representations tied to ego-motion. In *Proceedings of the IEEE International Conference on Computer Vision*, pages 1413–1421, 2015. 2
- [35] H. Jhuang, J. Gall, S. Zuffi, C. Schmid, and M. J. Black. Towards understanding action recognition. In *Proceedings of the IEEE international conference on computer vision*, pages 3192–3199, 2013. 5, 7
- [36] W. Kay, J. Carreira, K. Simonyan, B. Zhang, C. Hillier, S. Vijayanarasimhan, F. Viola, T. Green, T. Back, P. Natsev, M. Suleyman, and A. Zisserman. The kinetics human action video dataset. *arXiv preprint arXiv:1705.06950*, 2017. 1, 5
- [37] A. Khoreva, F. Perazzi, R. Benenson, B. Schiele, and A. Sorkine-Hornung. Learning video object segmentation from static images. *CoRR*, abs/1612.02646, 2016. 6
- [38] D. P. Kingma and J. Ba. Adam: A method for stochastic optimization. *arXiv preprint arXiv:1412.6980*, 2014. 5
- [39] S. Kong and C. Fowlkes. Image reconstruction with predictive filter flow. *arXiv preprint arXiv:1811.11482*, 2018. 2, 3
- [40] S. Kong and C. Fowlkes. Recurrent pixel embedding for instance grouping. In *Proceedings of the IEEE Conference on Computer Vision and Pattern Recognition (CVPR)*, pages 9018–9028, 2018. 8, 13
- [41] G. Larsson, M. Maire, and G. Shakhnarovich. Colorization as a proxy task for visual understanding. In *Proceedings of the IEEE Conference on Computer Vision and Pattern Recognition*, pages 6874–6883, 2017. 2
- [42] S. Lazebnik, C. Schmid, and J. Ponce. Semi-local affine parts for object recognition. In *British Machine Vision Conference (BMVC'04)*, pages 779–788. The British Machine Vision Association (BMVA), 2004. 2
- [43] A. Levin, Y. Weiss, F. Durand, and W. T. Freeman. Understanding and evaluating blind deconvolution algorithms. In *2009 IEEE Conference on Computer Vision and Pattern Recognition*, pages 1964–1971. IEEE, 2009. 2
- [44] C. Levy and T. Roosendaal. Sintel. In *ACM SIGGRAPH ASIA 2010 Computer Animation Festival, Seoul, Republic of Korea, December 15 - 18, 2010*, page 82:1, 2010. 5
- [45] C. Li, S. Su, Y. Matsushita, K. Zhou, and S. Lin. Bayesian depth-from-defocus with shading constraints. In *Proceedings of the IEEE Conference on Computer Vision and Pattern Recognition*, pages 217–224, 2013. 2
- [46] C. Liu et al. *Beyond pixels: exploring new representations and applications for motion analysis*. PhD thesis, Massachusetts Institute of Technology, 2009. 5, 6, 7
- [47] K.-K. Maninis, J. Pont-Tuset, P. Arbeláez, and L. Van Gool. Convolutional oriented boundaries: From image segmentation to high-level tasks. *IEEE transactions on pattern analysis and machine intelligence*, 40(4):819–833, 2018. 6
- [48] D. R. Martin, C. C. Fowlkes, and J. Malik. Learning to detect natural image boundaries using local brightness, color, and texture cues. *IEEE Transactions on Pattern Analysis & Machine Intelligence*, (5):530–549, 2004. 6
- [49] X. Mei, X. Sun, W. Dong, H. Wang, and X. Zhang. Segment-tree based cost aggregation for stereo matching. In *Proceedings of the IEEE Conference on Computer Vision and Pattern Recognition*, pages 313–320, 2013. 2
- [50] S. Meister, J. Hur, and S. Roth. Unflow: Unsupervised learning of optical flow with a bidirectional census loss. In *Thirty-Second AAAI Conference on Artificial Intelligence*, 2018. 1, 2, 4
- [51] M. Menze, C. Heipke, and A. Geiger. Discrete optimization for optical flow. In *German Conference on Pattern Recognition*, pages 16–28. Springer, 2015. 2
- [52] B. Mildenhall, J. T. Barron, J. Chen, D. Sharlet, R. Ng, and R. Carroll. Burst denoising with kernel prediction networks. In *Proceedings of the IEEE Conference on Computer Vision and Pattern Recognition*, pages 2502–2510, 2018. 2
- [53] I. Misra, C. L. Zitnick, and M. Hebert. Shuffle and learn: unsupervised learning using temporal order verification. In *European Conference on Computer Vision*, pages 527–544. Springer, 2016. 2, 8

- [54] M. K. Moore, R. Borton, and B. L. Darby. Visual tracking in young infants: Evidence for object identity or object permanence? *Journal of Experimental Child Psychology*, 25(2):183–198, 1978. [1](#)
- [55] A. A. Muller and R. N. Aslin. Visual tracking as an index of the object concept. *Infant Behavior and Development*, 1:309–319, 1978. [1](#)
- [56] V. Nair and G. E. Hinton. Rectified linear units improve restricted boltzmann machines. In *Proceedings of the 27th international conference on machine learning (ICML-10)*, pages 807–814, 2010. [5](#)
- [57] R. A. Newcombe, D. Fox, and S. M. Seitz. Dynamicfusion: Reconstruction and tracking of non-rigid scenes in real-time. In *Proceedings of the IEEE conference on computer vision and pattern recognition*, pages 343–352, 2015. [2](#)
- [58] A. Newell, Z. Huang, and J. Deng. Associative embedding: End-to-end learning for joint detection and grouping. In *Advances in Neural Information Processing Systems*, pages 2277–2287, 2017. [13](#)
- [59] S. Niklaus, L. Mai, and F. Liu. Video frame interpolation via adaptive convolution. In *Proceedings of the IEEE Conference on Computer Vision and Pattern Recognition*, pages 670–679, 2017. [2](#)
- [60] S. Niklaus, L. Mai, and F. Liu. Video frame interpolation via adaptive separable convolution. In *Proceedings of the IEEE International Conference on Computer Vision*, pages 261–270, 2017. [8](#)
- [61] M. Noroozi and P. Favaro. Unsupervised learning of visual representations by solving jigsaw puzzles. In *European Conference on Computer Vision*, pages 69–84. Springer, 2016. [2](#)
- [62] A. Owens, J. Wu, J. H. McDermott, W. T. Freeman, and A. Torralba. Ambient sound provides supervision for visual learning. In *European conference on computer vision*, pages 801–816. Springer, 2016. [2](#)
- [63] A. Paszke, S. Gross, S. Chintala, G. Chanan, E. Yang, Z. DeVito, Z. Lin, A. Desmaison, L. Antiga, and A. Lerer. Automatic differentiation in pytorch. 2017. [5](#)
- [64] D. Pathak, R. Girshick, P. Dollár, T. Darrell, and B. Hariharan. Learning features by watching objects move. In *Proceedings of the IEEE Conference on Computer Vision and Pattern Recognition*, pages 2701–2710, 2017. [2](#), [9](#)
- [65] D. Pathak, P. Krahenbuhl, J. Donahue, T. Darrell, and A. A. Efros. Context encoders: Feature learning by inpainting. In *Proceedings of the IEEE conference on computer vision and pattern recognition*, pages 2536–2544, 2016. [2](#)
- [66] D. Perrone and P. Favaro. A clearer picture of total variation blind deconvolution. *IEEE transactions on pattern analysis and machine intelligence*, 38(6):1041–1055, 2016. [2](#)
- [67] L. Pinto, D. Gandhi, Y. Han, Y.-L. Park, and A. Gupta. The curious robot: Learning visual representations via physical interactions. In *European Conference on Computer Vision*, pages 3–18. Springer, 2016. [2](#)
- [68] T. Pohlen, A. Hermans, M. Mathias, and B. Leibe. Full-resolution residual networks for semantic segmentation in street scenes. In *Proceedings of the IEEE Conference on Computer Vision and Pattern Recognition*, pages 4151–4160, 2017. [5](#), [13](#)
- [69] J. Pont-Tuset, F. Perazzi, S. Caelles, P. Arbeláez, A. Sorkine-Hornung, and L. Van Gool. The 2017 davis challenge on video object segmentation. *arXiv preprint arXiv:1704.00675*, 2017. [5](#), [6](#)
- [70] K. R. Popper. The arrow of time. *Nature*, 177(4507):538, 1956. [1](#)
- [71] A. Ranjan and M. J. Black. Optical flow estimation using a spatial pyramid network. In *Proceedings of the IEEE Conference on Computer Vision and Pattern Recognition*, pages 4161–4170, 2017. [7](#)
- [72] S. N. Ravi, Y. Xiong, L. Mukherjee, and V. Singh. Filter flow made practical: Massively parallel and lock-free. In *Proceedings of the IEEE Conference on Computer Vision and Pattern Recognition*, pages 3549–3558, 2017. [2](#)
- [73] Z. Ren, J. Yan, B. Ni, B. Liu, X. Yang, and H. Zha. Unsupervised deep learning for optical flow estimation. In *Thirty-First AAAI Conference on Artificial Intelligence*, 2017. [1](#), [4](#)
- [74] J. Revaud, P. Weinzaepfel, Z. Harchaoui, and C. Schmid. Epicflow: Edge-preserving interpolation of correspondences for optical flow. In *Proceedings of the IEEE conference on computer vision and pattern recognition*, pages 1164–1172, 2015. [2](#)
- [75] H. Rhodin, M. Salzmann, and P. Fua. Unsupervised geometry-aware representation for 3d human pose estimation. In *Proceedings of the European Conference on Computer Vision (ECCV)*, pages 750–767, 2018. [1](#)
- [76] O. Rippel, S. Nair, C. Lew, S. Branson, A. G. Anderson, and L. Bourdev. Learned video compression. *arXiv preprint arXiv:1811.06981*, 2018. [8](#)
- [77] O. Ronneberger, P. Fischer, and T. Brox. U-net: Convolutional networks for biomedical image segmentation. In *International Conference on Medical image computing and computer-assisted intervention*, pages 234–241. Springer, 2015. [5](#), [13](#)
- [78] D. Scharstein and R. Szeliski. A taxonomy and evaluation of dense two-frame stereo correspondence algorithms. *International journal of computer vision*, 47(1-3):7–42, 2002. [2](#)
- [79] S. M. Seitz and S. Baker. Filter flow. In *Proceedings of the IEEE Conference on Computer Vision and Pattern Recognition (CVPR)*, 2009. [2](#), [3](#)
- [80] P. Sermanet, C. Lynch, Y. Chebotar, J. Hsu, E. Jang, S. Schaal, S. Levine, and G. Brain. Time-contrastive networks: Self-supervised learning from video. In *2018 IEEE International Conference on Robotics and Automation (ICRA)*, pages 1134–1141. IEEE, 2018. [1](#)
- [81] E. P. Simoncelli. Bayesian multi-scale differential optical flow. 1999. [4](#)
- [82] K. Simonyan and A. Zisserman. Two-stream convolutional networks for action recognition in videos. In *Advances in neural information processing systems*, pages 568–576, 2014. [5](#), [8](#), [13](#)
- [83] N. Skafted, O. Freifeld, and S. Hauberg. Deep diffeomorphic transformer networks. In *Proceedings of the*

- IEEE Conference on Computer Vision and Pattern Recognition*, pages 4403–4412, 2018. 1
- [84] J. Song, L. Wang, L. Van Gool, and O. Hilliges. Thin-slicing network: A deep structured model for pose estimation in videos. In *Proceedings of the IEEE Conference on Computer Vision and Pattern Recognition*, pages 4220–4229, 2017. 7
- [85] R. Szeliski. *Bayesian modeling of uncertainty in low-level vision*, volume 79. Springer Science & Business Media, 2012. 4
- [86] U. Trottenberg, C. W. Oosterlee, and A. Schuller. *Multigrid*. Elsevier, 2000. 2, 3, 4
- [87] H.-Y. Tung, H.-W. Tung, E. Yumer, and K. Fragkiadaki. Self-supervised learning of motion capture. In *Advances in Neural Information Processing Systems*, pages 5236–5246, 2017. 1, 2
- [88] S. Vijayanarasimhan, S. Ricco, C. Schmid, R. Sukthankar, and K. Fragkiadaki. Sfm-net: Learning of structure and motion from video. *arXiv preprint arXiv:1704.07804*, 2017. 1
- [89] C. Von Hofsten, O. Kochukhova, and K. Rosander. Predictive tracking over occlusions by 4-month-old infants. *Developmental Science*, 10(5):625–640, 2007. 1
- [90] C. Vondrick, H. Pirsiavash, and A. Torralba. Generating videos with scene dynamics. In *Advances In Neural Information Processing Systems*, pages 613–621, 2016. 2
- [91] C. Vondrick, A. Shrivastava, A. Fathi, S. Guadarrama, and K. Murphy. Tracking emerges by colorizing videos. In *Proceedings of the European Conference on Computer Vision (ECCV)*, pages 391–408, 2018. 1, 2, 5, 6, 7, 9, 13
- [92] X. Wang and A. Gupta. Unsupervised learning of visual representations using videos. In *Proceedings of the IEEE International Conference on Computer Vision*, pages 2794–2802, 2015. 2
- [93] X. Wang, K. He, and A. Gupta. Transitive invariance for self-supervised visual representation learning. In *Proceedings of the IEEE International Conference on Computer Vision*, pages 1329–1338, 2017. 2
- [94] X. Wang, A. Jabri, and A. A. Efros. Learning correspondence from the cycle-consistency of time. *arXiv preprint arXiv:1903.07593*, 2019. 2, 5, 6, 7, 8, 9, 13
- [95] Y. Wang, Y. Yang, Z. Yang, L. Zhao, P. Wang, and W. Xu. Occlusion aware unsupervised learning of optical flow. In *Proceedings of the IEEE Conference on Computer Vision and Pattern Recognition*, pages 4884–4893, 2018. 1, 2, 4, 7
- [96] D. Wei, J. J. Lim, A. Zisserman, and W. T. Freeman. Learning and using the arrow of time. In *Proceedings of the IEEE Conference on Computer Vision and Pattern Recognition*, pages 8052–8060, 2018. 1, 2, 8
- [97] J. Wu, J. J. Lim, H. Zhang, J. B. Tenenbaum, and W. T. Freeman. Physics 101: Learning physical object properties from unlabeled videos. In *BMVC*, volume 2, page 7, 2016. 2
- [98] C. Xie, Y. Xiang, D. Fox, and Z. Harchaoui. Object discovery in videos as foreground motion clustering. *arXiv preprint arXiv:1812.02772*, 2018. 9
- [99] L. Yang, Y. Wang, X. Xiong, J. Yang, and A. K. Katsaggelos. Efficient video object segmentation via network modulation. In *Proceedings of the IEEE Conference on Computer Vision and Pattern Recognition*, pages 6499–6507, 2018. 6
- [100] Y. Yang and D. Ramanan. Articulated human detection with flexible mixtures of parts. *IEEE transactions on pattern analysis and machine intelligence*, 35(12):2878–2890, 2013. 7
- [101] Z. Yang, P. Wang, Y. Wang, W. Xu, and R. Nevatia. Every pixel counts: Unsupervised geometry learning with holistic 3d motion understanding. In *European Conference on Computer Vision*, pages 691–709. Springer, 2018. 1, 8
- [102] R. Yu, C. Russell, N. D. Campbell, and L. Agapito. Direct, dense, and deformable: Template-based non-rigid 3d reconstruction from rgb video. In *Proceedings of the IEEE International Conference on Computer Vision*, pages 918–926, 2015. 2
- [103] H. Zhan, R. Garg, C. Saroj Weerasekera, K. Li, H. Agarwal, and I. Reid. Unsupervised learning of monocular depth estimation and visual odometry with deep feature reconstruction. In *Proceedings of the IEEE Conference on Computer Vision and Pattern Recognition*, pages 340–349, 2018. 1
- [104] R. Zhang, P. Isola, and A. A. Efros. Split-brain autoencoders: Unsupervised learning by cross-channel prediction. In *Proceedings of the IEEE Conference on Computer Vision and Pattern Recognition*, pages 1058–1067, 2017. 2
- [105] T. Zhou, M. Brown, N. Snavely, and D. G. Lowe. Unsupervised learning of depth and ego-motion from video. In *Proceedings of the IEEE Conference on Computer Vision and Pattern Recognition*, pages 1851–1858, 2017. 1, 2
- [106] T. Zhou, P. Krahenbuhl, M. Aubry, Q. Huang, and A. A. Efros. Learning dense correspondence via 3d-guided cycle consistency. In *Proceedings of the IEEE Conference on Computer Vision and Pattern Recognition*, pages 117–126, 2016. 2
- [107] T. Zhou, S. Tulsiani, W. Sun, J. Malik, and A. A. Efros. View synthesis by appearance flow. In *European conference on computer vision*, pages 286–301. Springer, 2016. 2
- [108] B. Zoph and Q. V. Le. Neural architecture search with reinforcement learning. *arXiv preprint arXiv:1611.01578*, 2016. 13

Appendix

In the appendix, we first show all intermediate results of multigrid Predictive Filter Flow (mgPFF) from multi-resolution inputs, to have an idea how these outputs look like in terms of frame reconstruction. Then, we plot the graph visualization of our model architecture with detailed design of the two stream architecture. Furthermore, we visualize pixel embedding generated by our architecture to understand what the model learns. Finally, along this document, we provide some demo videos of the object segmentation/tracking results with different setup.

1. Intermediate Reconstruction by mgPFF

As our mgPFF performs progressively from coarse to fine, it produces the predicted filter flows and reconstruction frames at each resolution scale. We visualize all the intermediate results in Fig. 7. We also accumulate the filter flow maps at all scales and convert it into the coordinate flow, which can be thought as optical flow. We use this coordinate flow to warp masks for propagating the track results in our experiments. Please pay attention to how mgPFF achieves excellent reconstruction results from coarse to fine, like resolving the aliasing and block effects, refining reconstruction at finer scales, etc.

2. Graph Visualization of mgPFF architecture

In Fig. 8, we plot the architecture of our model using the HiddenLayer toolbox [1]. As the visualization is too “long” to display, we chop it into four parts. We modify the ResNet18 [25] by removing res_4 and res_5 (the top 9 residual blocks, and reducing the unique channel size from [64, 128, 256, 512] to [32, 64, 128, 196]. The two macro towers take the two frames, respectively; in each tower, there are two streams, one is of U-shape [77] with pooling and upsampling layers to increase the receptive fields, the other is full-resolution yet shallow in channel depth. The two-stream architecture is popular in multiple domain learning [82], but we note that such design on a single domain was first used in [68] which is more computationally expensive than the two streams talk to each other along the whole network flow; whereas ours is cheaper that they only talk at the top layer. Our mgPFF is very compact that the overall model size is only **4.6MB**; it also performs fast that the wall-clock time for processing a pair of 256x256 frames is 0.1 seconds.

As we did not search over architecture design in our work, it is worth exploring other sophisticated modules to make it more compact for deploying in mobile devices, e.g., using meta-learning for architecture search [108].

3. Pixel Embedding in mgPFF

As our model produces per-image pixel embeddings [58, 40] (the output before “concatenation layer” as shown in the architecture Fig. 8), we are interested in visualizing the pixel embeddings to see what the model learns. To visualize the pixel embeddings, we use PCA to project the embedding feature map $H \times W \times D$ at each resolution/grid into an $H \times W \times 3$ array, and visualize the projection as an RGB image. We also concatenate the embedding maps at all the resolutions/grids for visualization (with necessary nearest neighbor upsampling). Fig. 9 lists these visualizations, from which we can see the embedding colors largely come from the original RGB intensities. We conjecture this is due to two reasons. First, we use a simplistic photometric loss on the RGB values, this explains why the visualization colors group the pixels which have similar RGB values in local neighborhood. Second, our mgPFF by nature is based on low-level vision, i.e., flow field, and in such a way it does not necessarily depend on mid/high-level understanding of the frames. Therefore, part/instance grouping does not appear in the embedding visualization, which is shown in mid-level methods [91, 94]. This suggests further exploration of using other losses and combining other mid/high-level cues to force the model to learn more abstract features.

4. Video Demos

The attached videos demonstrate how mgPFF performs with different setup⁴. Note how it improves performance with different setup in terms of dealing with occlusion and large displacement.

Among the videos, it is worth noting how far the model can go with tracking correctly. As we adopt the multigrid computing strategy, the filter of size 11x11 on the coarsest grid (16x downsample) implies the largest displacement we can represent is $D=88$. If we simply warp from the first frame to the t^{th} frame, it only works well when the total displacement is less than D . This can be seen from video *soccerball, K=1, frame-[1]* as an example. When the soccerball moves further than D from its initial location at the first frame, the model suddenly fails in tracking that the mask is no longer correctly warped. We show the relevant frames in Fig. 10. It is clear that not only the tracking is missing, but also the filter flow changes abruptly and the reconstruction becomes very different. It turns out that in the reconstruction, the soccerball’s color is from the grass and tree trunk.

Here is the list of videos with brief description:

1. *soccerball, K=3, frame-[1, $t-2, t-1$]*: this video shows the results on soccerball from DAVIS dataset when we feed the **first frame-1 and two previous**

⁴Here is a [Youtube list](#)

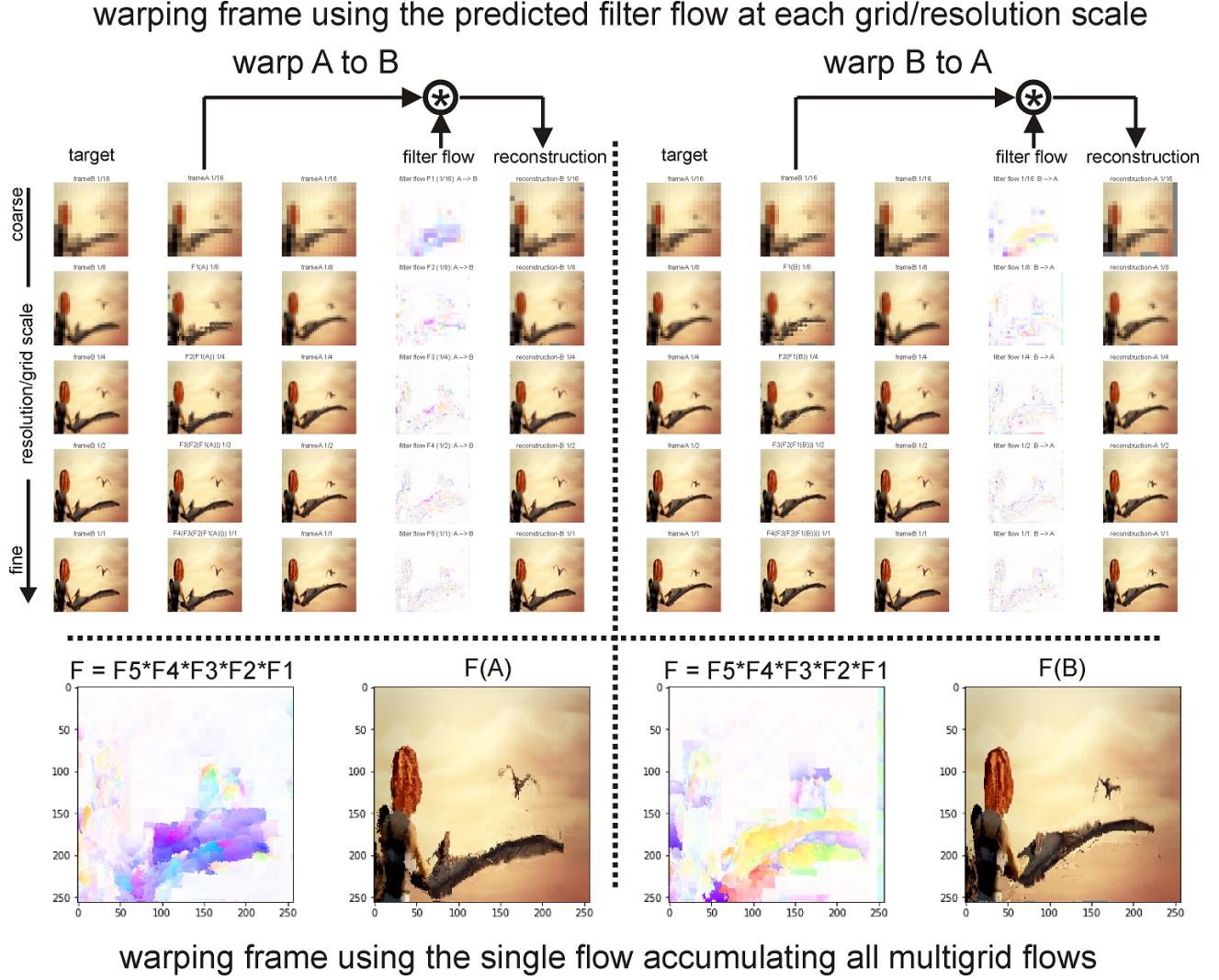


Figure 7: **Visualization of intermediate results at each resolution scale (grid).** Top: we show the predicted filter flows and the reconstruction results from warping A to B, or B to A. Note how mgPFF resolves the aliasing effect reflected by the blocks in the reconstruction images. Bottom: we accumulate all the filter flows (with necessary upsampling using nearest neighbor interpolation), and transform into a coordinate flow which can be thought as optical flow. Then we use the overall flow to warp from one frame to the other. This introduces some artifacts due to information loss, but the reconstruction appears good generally, e.g., capturing the bird wings' movement. In our experiment of tracking, we use the coordinate flow in the same way to warp the given masks (or the predicted mask at previous frames) to propagate the track results.

frame ($t - 2$ and $t - 1$) to predict the filter flow, warp frame and track the object at current frame- t . (video url <https://youtu.be/M49nLtT1UmY>).

2. *soccerball*, $K=3$, *frame*- $[t - 3, t - 2, t - 1]$: this video shows the results on soccerball from DAVIS dataset when we feed the **previous three frames** ($t - 3$, $t - 2$ and $t - 1$) to predict the filter flow, warp frame and track the object at current frame- t (video url https://youtu.be/q_FNk-3lh3g).

3. *soccerball*, $K=2$, *frame*- $[1, t - 1]$, this video shows

the results on soccerball from DAVIS dataset when we feed the **first frame-1 and one previous frame-** ($t - 1$) to predict the filter flow, warp frame and track the object. (video url <https://youtu.be/u6IdVS2L7-M>).

4. *soccerball*, $K=1$, *frame*- $[1]$, this video shows the results on soccerball from DAVIS dataset when we feed the **first frame only** at which the mask is given to predict the filter flow, warp frame and track the object. (video url <https://youtu.be/vsXZgdR4XEY>)

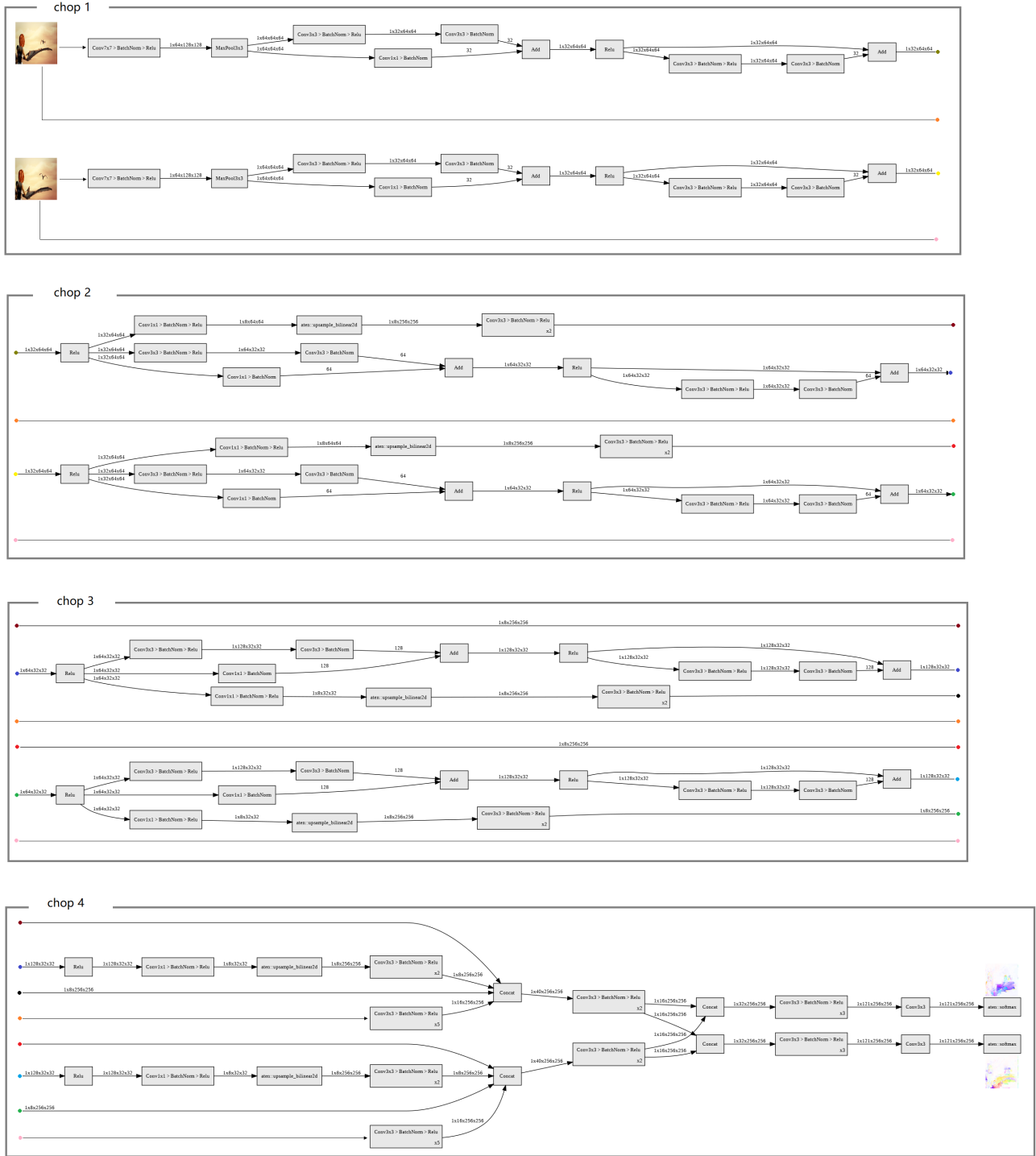


Figure 8: Graph visualization of mgPFF architecture using HiddenLayer toolbox [1]. Zoom in to see clearly.

5. *soccerball*, $K=1$, $frame-[t-1]$, this video shows the results on soccerball from DAVIS dataset when we feed the **the previous frame**-($t-1$) to predict the filter flow, warp frame and track the object at cur-

rent frame- t . (video url <https://youtu.be/8AZ9wPF15QE>)

6. *dog*, $K=3$, $frame-[1, t-2, t-1]$: this video shows

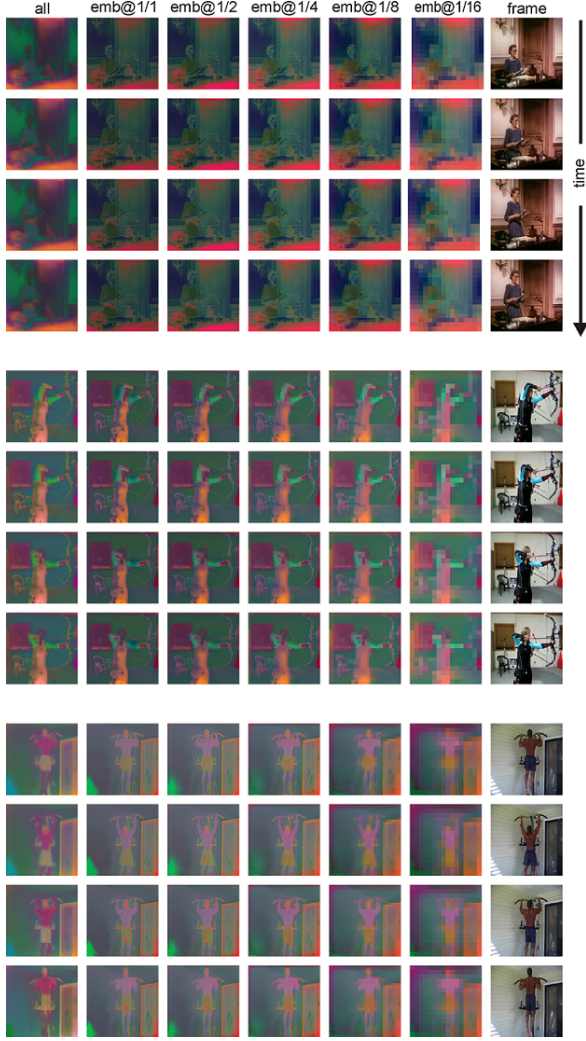


Figure 9: **Visualization of learned pixel embedding:** We use PCA to project the pixel embedding (3D array of size $H \times W \times D$) into $H \times W \times 3$, and visualize it as an RGB image. Individual embedding map has $D = 16$ in channel dimension. We also concatenate the pixel embeddings of all resolutions and apply PCA, in which case $D = 16 * 5 = 80$. From the visualization, we can see that the visualization colors largely come from the RGB intensities. This is largely due to two reasons: 1) the photometric loss we are using during training is based on RGB intensities, 2) our mgPFF by nature is based on low-level vision that it does not need understanding of mid/high-level perspective of the frames.

the results on dog from DAVIS dataset when we feed the **first frame-1 and two previous frame** ($t - 2$ and $t - 1$) to predict the filter flow, warp frame and track the object at current frame- t . (video url <https://youtu.be/seg5tFSMFx8>).

7. *dog*, $K=3$, $frame-[t-3, t-2, t-1]$: this video shows the results on dog from DAVIS dataset when we feed the **previous three frames** ($t - 3$, $t - 2$

and $t - 1$) to predict the filter flow, warp frame and track the object at current frame- t (video url <https://youtu.be/BqM4-OctYwA>).

8. *dog*, $K=2$, $frame-[1, t-1]$, this video shows the results on dog from DAVIS dataset when we feed the **first frame-1 and one previous frame**-($t - 1$) to predict the filter flow, warp frame and track the object. (video url <https://youtu.be/dOao8qQMsv0>).
9. *dog*, $K=1$, $frame-[1]$, this video shows the results on dog from DAVIS dataset when we feed the **first frame only** at which the mask is given to predict the filter flow, warp frame and track the object. (video url <https://youtu.be/xNMuMlcvfJY>)
10. *dog*, $K=1$, $frame-[t-1]$, this video shows the results on dog from DAVIS dataset when we feed the **the previous frame**-($t - 1$) to predict the filter flow, warp frame and track the object at current frame- t . (video url <https://youtu.be/Yu5amZf1KEc>)

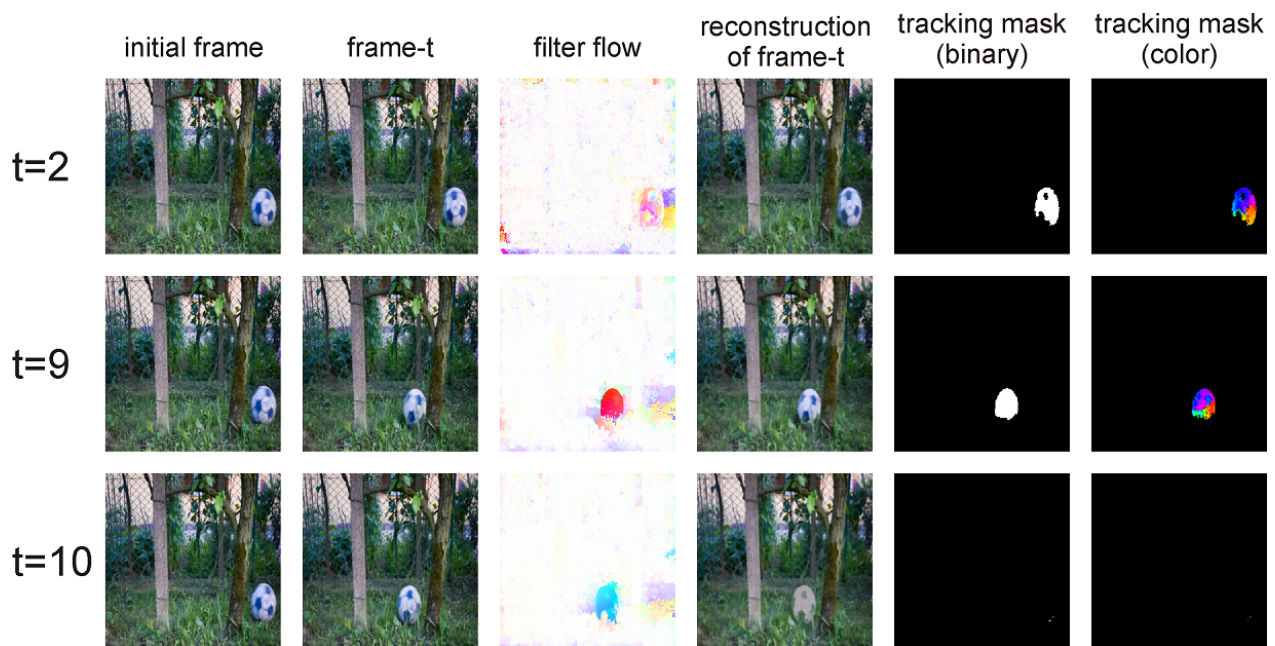


Figure 10: How far the model can track the object correctly? As we adopt the multigrid computing strategy, the filter of size 11×11 on the coarsest grid (16x downsample) implies the largest displacement we can represent is $D=88$. If the object moves further than D from its last location, the model fails in tracking it. This happens at frame-10, in which we can see that not only the tracking is missing, but also the filter flow changes abruptly and the reconstruction becomes very different. It turns out that in the reconstruction, the soccerball's color is from the grass and tree trunk.